




# Primary cilia control glucose homeostasis via islet paracrine interactions

Jing W. Hughes<sup>a,1</sup> , Jung Hoon Cho<sup>a</sup>, Hannah E. Conway<sup>a</sup>, Michael R. DiGrucio<sup>b</sup>, Xue Wen Ng<sup>b</sup>, Henry F. Roseman<sup>a</sup>, Damien Abreu<sup>a</sup>, Fumihiko Urano<sup>a</sup>, and David W. Piston<sup>b</sup>

<sup>a</sup>Department of Medicine, Washington University School of Medicine, St. Louis, MO 63110; and <sup>b</sup>Department of Cell Biology and Physiology, Washington University School of Medicine, St. Louis, MO 63110

Edited by C. Ronald Kahn, Harvard Medical School, Boston, MA, and approved March 10, 2020 (received for review January 31, 2020)

**Pancreatic islets regulate glucose homeostasis through coordinated actions of hormone-secreting cells. What underlies the function of the islet as a unit is the close approximation and communication among heterogeneous cell populations, but the structural mediators of islet cellular cross talk remain incompletely characterized. We generated mice specifically lacking  $\beta$ -cell primary cilia, a cellular organelle that has been implicated in regulating insulin secretion, and found that the  $\beta$ -cell cilia are required for glucose sensing, calcium influx, insulin secretion, and cross regulation of  $\alpha$ - and  $\delta$ -cells. Protein expression profiling in islets confirms perturbation in these cellular processes and reveals additional targets of cilia-dependent signaling. At the organism level, the deletion of  $\beta$ -cell cilia disrupts circulating hormone levels, impairs glucose homeostasis and fuel usage, and leads to the development of diabetes. Together, these findings demonstrate that primary cilia not only orchestrate  $\beta$ -cell-intrinsic activity but also mediate cross talk both within the islet and from islets to other metabolic tissues, thus providing a unique role of cilia in nutrient metabolism and insight into the pathophysiology of diabetes.**

The pancreatic islet secretes hormones required for metabolic homeostasis. Common to all forms of diabetes are a relative or absolute insulin deficiency and metabolic imbalance associated with  $\beta$ -cell dysfunction (1). Islet hormone secretion is a dynamic process determined by not only cell-intrinsic properties, e.g., ion channels, but also cell–cell connectivity and communication (2, 3). Primary cilia are a unique regulator of islet cells; a single primary cilium protrudes from each cell body and occupies the common luminal space between neighboring islet cells (4, 5). These hairlike organs are rich with G protein-coupled receptors (GPCRs) and chemosensory receptors and act as a signaling hub to direct cellular functions. Structurally, IFT88 is a component of the intraflagellar transport (IFT) complex and is required for cilia assembly (6, 7). Loss of IFT88 causes the absence of cilia and leads to cystic kidney disease in both mice and humans (8, 9).

Primary cilia have been shown to regulate insulin secretion (10), but it is unclear which events during  $\beta$ -cell glucose-stimulated insulin secretion are under cilia control and how this relates to whole-body physiology. A high incidence of obesity and diabetes is found in two human ciliopathies, Bardet–Biedl and Alström syndromes (11, 12). The pathophysiology of cilia-related diabetes is incompletely understood and likely encompasses combined effects on feeding behavior, pancreatic development, and glucose handling. Most animal models of ciliopathy-related diabetes to date have been global or whole-pancreas knockouts with mixed phenotypes that cannot be attributed to defects in any specific tissue or cell type (10, 13, 14). Accordingly, there is a lack of mechanistic understanding of cilia-dependent regulation of the endocrine pancreas.

To specifically examine the role of cilia in  $\beta$ -cell and islet function, we generated an *Ins1-Cre*  $\beta$ -cell cilia knockout ( $\beta$ CKO) mouse and studied its phenotype at the cellular, tissue, and organismal level. We find that targeted deletion of  $\beta$ -cell cilia causes not only  $\beta$ -cell secretory failure, as also seen in a recent *Pdx1-Cre* cilia KO model (15), but also aberrant  $\alpha$ - and  $\delta$ -cell hormone secretion and altered systemic energy metabolism. Our studies implicate primary cilia as a key regulator of glucose-sensing,

cellular synchronicity, and both intra- and intercellular signaling pathways that govern core islet functions, demonstrating that primary cilia are required for islet function as a unit and for the maintenance of energy homeostasis.

## Results

**INS1-Cre/IFT88-Flox Mice Lack  $\beta$ -Cell Cilia.** To determine the role of primary cilia in  $\beta$ -cell function, we generated  $\beta$ CKO mice by crossing *INS1-Cre* (16) with *IFT88-Flox* mice (17). The *INS1-Cre* strain was chosen based on efficient and selective recombination in  $\beta$ -cells and established lack of expression in the central nervous system (16). A parallel tamoxifen-inducible line,  $\beta$ CKO-ERT2, was generated by crossing *IFT88-Flox* with *INS1-CreERT2* (16) and was used as a control. Both  $\beta$ CKO and  $\beta$ CKO-ERT2 mice are on the C57BL/6 background, are fertile and carry normal-size litters in Mendelian ratios, and produce pups with no obvious developmental defects at the time of weaning.

Successful cilia knockout was confirmed using immunohistochemistry, qPCR, and immunoblotting. To visualize primary cilia morphology and distribution in normal islets, we stained healthy human and mouse islets with three independent cilia markers, including *Arl13b*, polyglutamylated tubulin, and acetylated  $\alpha$ -tubulin (Fig. 1*A* and *C*). We also captured an electron micrograph of a human  $\beta$ -cell cilium in ultrastructural detail (Fig. 1*B*). Compared to wild-type (WT) mice,  $\beta$ CKO mice lack cilia exclusively on islet  $\beta$ -cells (Fig. 1*C*), with deletion of *IFT88* gene expression confirmed by qPCR (Fig. 1*D*) and by immunoblot of *IFT88* (Fig. 1*E*). Residual

## Significance

The primary cilium is a small subcompartment of the cell but has powerful influence on pancreatic islet function. In this study, we find a critical role for cilia in regulating  $\beta$ -cell function and energy metabolism. Importantly, the deletion of  $\beta$ -cell cilia disrupts intercellular communication and leads to islet dysfunction and diabetes, as seen in a number of human ciliopathy syndromes. These results should help elucidate pathophysiology of human ciliopathy and aid the development of pharmacologic agents targeting primary cilia that may lead to a more effective treatment for human diabetes.

Author contributions: J.W.H. and D.W.P. designed research; J.W.H., J.H.C., H.E.C., M.R.D., X.W.N., and H.F.R. performed research; F.U. and D.W.P. contributed new reagents/analytic tools; J.H.C., M.R.D., X.W.N., and D.A. analyzed data; and J.W.H. wrote the paper.

The authors declare no competing interest.

This article is a PNAS Direct Submission.

This open access article is distributed under [Creative Commons Attribution-NonCommercial-NoDerivatives License 4.0 \(CC BY-NC-ND\)](https://creativecommons.org/licenses/by-nc-nd/4.0/).

Data deposition: Any data and materials that can be shared will be released via a Materials Transfer Agreement. The phosphoprotein and signaling array data have been deposited in the Gene Expression Omnibus under accession numbers [GSE138856](https://www.ncbi.nlm.nih.gov/geo/query/acc.cgi?acc=GSE138856) and [GSE138885](https://www.ncbi.nlm.nih.gov/geo/query/acc.cgi?acc=GSE138885).

<sup>1</sup>To whom correspondence may be addressed. Email: [jing.hughes@wustl.edu](mailto:jing.hughes@wustl.edu).

This article contains supporting information online at <https://www.pnas.org/lookup/suppl/doi:10.1073/pnas.2001936117/-DCSupplemental>.

First published April 6, 2020.

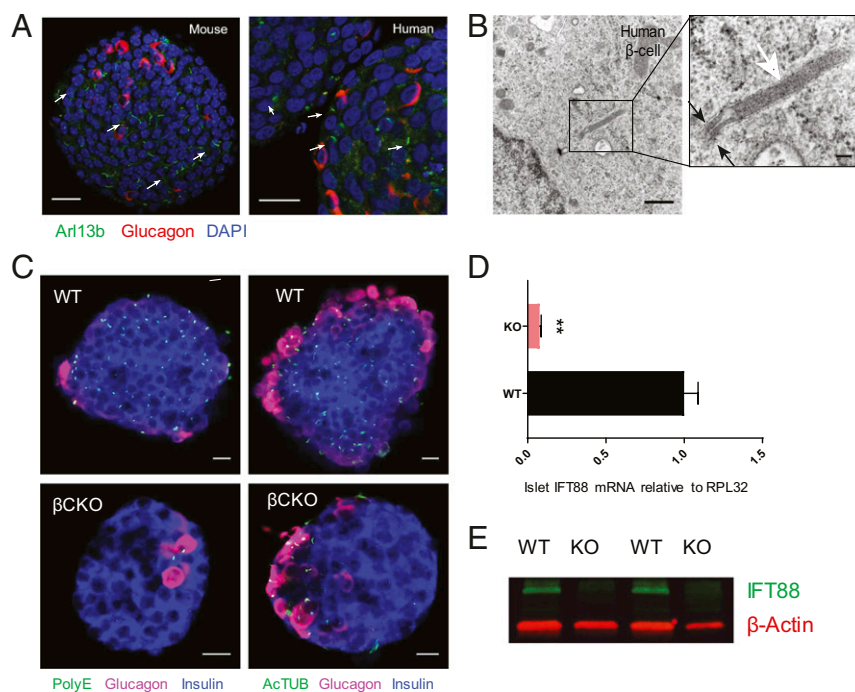


**Fig. 1.** INS1-Cre/IFT88-Flox islets lack  $\beta$ -cell cilia. (A) Normal mouse and human islets have ciliated  $\alpha$ -cells and  $\beta$ -cells (majority of non- $\alpha$ -cells). Arl13b, cilia GTPase; Glucagon,  $\alpha$ -cell marker; DAPI, nucleus marker. (Scale bar, 20  $\mu$ m.) White arrows indicate cilia. (B) Ultrastructural examination of human islets from a healthy young male reveals a single  $\beta$ -cell primary cilium, with an intact axoneme (white arrow) and basal bodies (black arrows). (Scale bar, 600 nm, main panel; 100 nm, *Inset*). (C) INS1-Cre IFT88 knockout ( $\beta$ CKO) mice lack cilia specifically on  $\beta$ -cells, as detected by costaining of insulin and polyglutamylated tubulin (PolyE, GT335) or acetylated  $\alpha$ -tubulin (AcTUB). (Scale bar, 10  $\mu$ m.) Images are representative of three experiments with four mice each. (D) IFT88 gene expression is abolished in KO islets.  $**P = 0.0093$ . RPL32, housekeeping control.  $n = 4$  mice per genotype. (E) IFT88 protein expression is diminished in KO islets.  $\beta$ -actin, loading control. Shown are four individual mice; results are representative of three experiments.

IFT88 expression in knockout islets was likely from  $\alpha$ -cells and other non- $\beta$ -cells. As a control, we induced  $\beta$ -cell cilia knockout by treating  $\beta$ CKO-ERT2 mice with tamoxifen and showed that this depleted cilia in adult islet  $\beta$ -cells and induced hyperglycemia and glucose intolerance within days of treatment (*SI Appendix, Fig. S1*). Primary cilia expression on  $\beta$ CKO-ERT2 islet  $\alpha$ -cells and other non- $\beta$ -cells was unaffected by tamoxifen, confirming  $\beta$ -cell specificity of Cre-ERT2 recombination.

#### Inactivation of $\beta$ -Cell Cilia Leads to Altered Islet Composition.

Whereas  $\beta$ -cells comprise the predominant cell type in normal mouse islets, deletion of  $\beta$ -cell cilia resulted in altered islet cellular composition. Flow sorting by FluoZin3 (18) shows that KO islets contain a lower percentage of functional  $\beta$ -cells ( $66.9 \pm 5.1\%$  KO,  $88.4 \pm 6.5\%$  WT; Fig. 2A). Whole-pancreas sections from 8-wk-old  $\beta$ CKO mice reveal normal islet area and circularity scores (Fig. 2B and C), while  $\beta$ -cell mass as assessed by insulin-positive areas was decreased (Fig. 2D). Total insulin content is also lower in KO islets ( $379 \pm 47.9$  ng/10 islets KO,  $480 \pm 36.5$  ng/10 islets WT; Fig. 2E), while  $\alpha$ -cell mass and glucagon content are not significantly different between WT and KO ( $903 \pm 124$  ng/10 islets KO,  $853 \pm 82$  pg/10 islets WT).  $\delta$ -cell mass and somatostatin content are significantly increased in KO ( $756 \pm 101$  ng/10 islets KO,  $409 \pm 70$  pg/10 islets WT; Fig. 2D and E). Despite grossly normal islet architecture seen on paraffin sections,  $\beta$ CKO islets have altered intraislet collagen deposition and increased E-cadherin expression (*SI Appendix, Fig. S2*), suggesting altered cellular connectivity.

**Primary Cilia Mediate Paracrine Regulation of Islet Cells.** The secretory function of  $\beta$ CKO islets was examined in both static and dynamic settings, revealing changes in hormone output from all major islet cell types. During static incubation when glucose

concentration is raised from 1 to 11 mM,  $\beta$ CKO islets exhibit impaired glucose-stimulated insulin secretion (Fig. 3A, *Left*, fold induction of  $1.69 \pm 0.38$  KO vs.  $7.44 \pm 0.48$  WT). This difference in secretion capacity exceeds what would be expected from the modest reduction in  $\beta$ -cell mass (Fig. 2D), suggesting impairment in the actual  $\beta$ -cell secretory process. Dynamic secretion experiments reveal blunted first-phase insulin secretion to glucose challenge and slower recovery to baseline in KO compared to WT islets, a phenotype suggestive of  $\beta$ -cell asynchrony (19) (Fig. 3B). To confirm that cilia deletion and not developmental changes directly disrupts  $\beta$ -cell insulin secretion, we induced cilia knockout in adult  $\beta$ CKO-ERT2 islets using tamoxifen. Repeat dynamic secretion experiments show that short-term ablation of primary cilia in islet  $\beta$ -cells diminishes first-phase insulin secretion (*SI Appendix, Fig. S1D*), recapitulating the defect seen in constitutive  $\beta$ CKO islets.

We observe a strong effect of  $\beta$ -cell cilia deficiency on  $\alpha$ -cell and  $\delta$ -cell hormone secretion, which reveals a role for islet cilia in cross regulating neighboring cells. Glucagon secretion is higher in  $\beta$ CKO islets under basal conditions at low glucose and is less inhibited by high glucose (Fig. 3A, *Middle*, fold suppression of  $1.75 \pm 0.62$  KO vs.  $4.97 \pm 0.56$  WT). Glucagon dynamic secretion by KO islets shows higher baseline and less glucose suppression compared to WT islets (Fig. 3C). Somatostatin response to glucose is also disrupted, as KO islets secrete 1.7-fold more somatostatin than WT islets at low glucose but exhibit damped induction by high glucose (Fig. 3A, *Right*, fold induction of  $1.80 \pm 0.54$  KO vs.  $2.44 \pm 0.63$  WT). Collectively, these changes indicate that  $\beta$ -cell cilia deficiency not only affects insulin release from the  $\beta$ -cell but also leads to an altered hormonal milieu in the local islet environment and reduced glucose response by islet cells en masse.

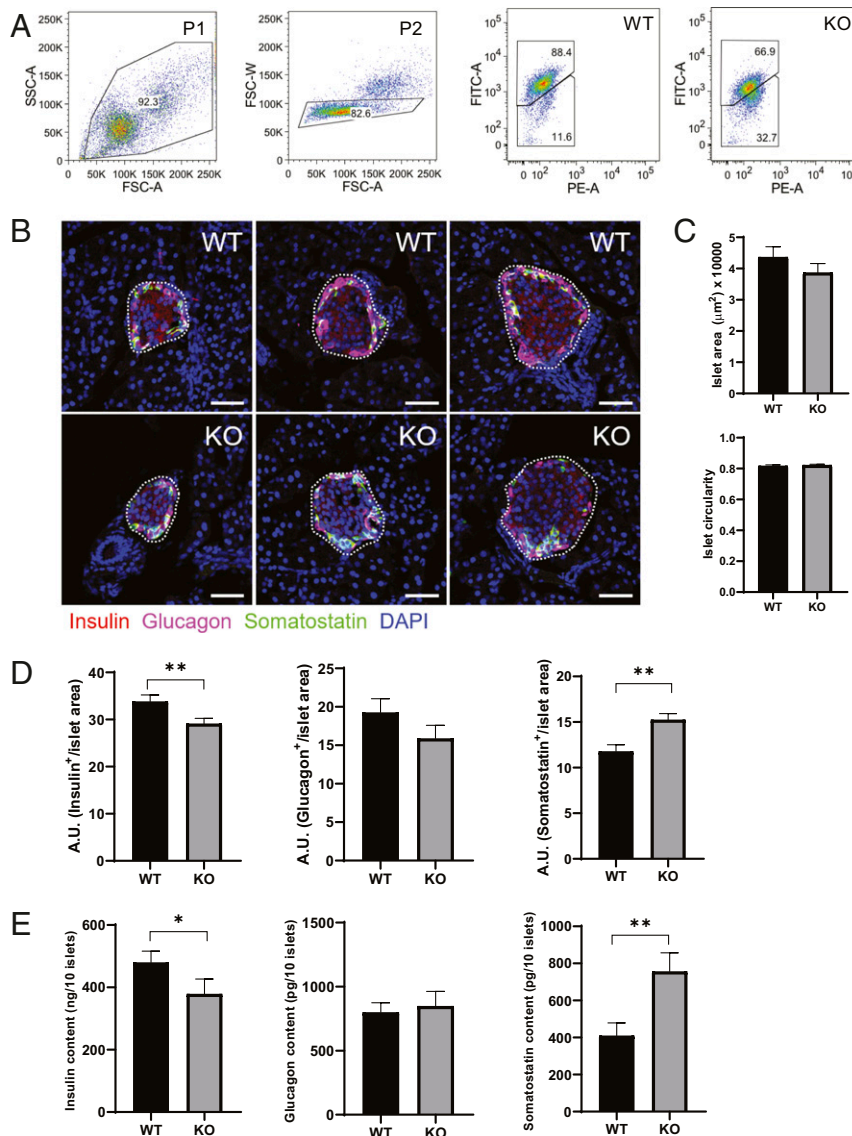


**Fig. 2.** Inactivation of  $\beta$ -cell cilia leads to altered islet composition. (A) Dispersed WT and  $\beta$ CKO islets are sorted after gating on SSC-A<sup>hi</sup>/FSC-A<sup>hi</sup> (P1, intact cells), FSC-W<sup>lo</sup>/FSC-A<sup>hi</sup> (P2, singlets), and FITC<sup>hi</sup> (FluoZin+  $\beta$ -cells). KO islets have a reduced abundance of  $\beta$ -cells compared to WT islets. Data are representative of three experiments,  $n = 500$  islets per experiment. (B) Insulin (red), glucagon (magenta), and somatostatin (green) immunostaining in whole pancreatic sections from WT and KO mice at 8 to 10 wk of age. (Scale bar, 50  $\mu\text{m}$ ). Images are representative of >200 sections examined. (C) WT and  $\beta$ CKO islets have comparable islet area ( $P = 0.268$ ) and islet circularity score ( $P = 0.659$ ). Additional morphometric data are shown in *SI Appendix, Fig. S2*. (D) Reduced insulin (\*\* $P = 0.0089$ ) and increased somatostatin (\*\* $P = 0.0011$ ) in  $\beta$ CKO islets as quantified by immunofluorescence. Glucagon trends low in KO islets but does not reach significance ( $P = 0.0747$ ).  $n = 265$  WT and 280 KO islets from six animals each. (E)  $\beta$ CKO islets have reduced total insulin content (\* $P = 0.0197$ ), normal glucagon content ( $P = 0.683$ ), and increased somatostatin content (\*\* $P = 0.0033$ ).  $n = 50$  or more groups of 10 islets examined in >10 experiments.

To examine the response of  $\beta$ CKO  $\beta$ -cells to paracrine cues, we measured insulin secretion in the presence of purified glucagon or somatostatin. Glucagon treatment augmented insulin secretion from  $\beta$ CKO islets in a dose-dependent manner, comparable to WT islets (Fig. 3D). In contrast, somatostatin treatment failed to inhibit insulin secretion by  $\beta$ CKO islets (Fig. 3E), suggesting that primary cilia mediate somatostatin responsiveness in  $\beta$ -cells. We also examined nonparacrine cues using recombinant EphA5-Fc or ephrin-A5-Fc to stimulate or inhibit the classic juxtacrine pathway known to mediate islet cell cross talk (20); however, this pathway appears to be independent of cilia regulation as WT and  $\beta$ CKO islets responded similarly in both insulin and glucagon secretion (Fig. 3F and G).

**Primary Cilia Regulate  $\beta$ -Cell  $\text{Ca}^{2+}$  Response to Glucose.** In both mouse and human islets,  $\beta$ -cell insulin secretion is triggered by

calcium ion influx. The normal  $\text{Ca}^{2+}$  activity in the  $\beta$ -cell is marked by an initial coordinated burst that corresponds to first-phase insulin secretion, followed by a period of sustained  $\text{Ca}^{2+}$  oscillations that corresponds to second-phase insulin secretion (21, 22). We hypothesized that the defective insulin secretion by  $\beta$ CKO mice is due to a loss of normal islet  $\text{Ca}^{2+}$  dynamics. To test this, we performed time-lapse imaging of glucose-stimulated islet calcium flux at cellular resolution.

Purified  $\beta$ CKO or WT islets were loaded with the  $\text{Ca}^{2+}$  indicator Fluo-4 AM and imaged while being stimulated with 8 mM glucose. Kymographs depicting  $\text{Ca}^{2+}$  response in individual cells across the volume of the islet show abnormal  $\beta$ -cell  $\text{Ca}^{2+}$  activation and dyssynchrony in KO islets (Fig. 4A and B). Notably, KO islet  $\text{Ca}^{2+}$  response lacks both the initial coordinated burst and the oscillatory behavior seen in WT islets

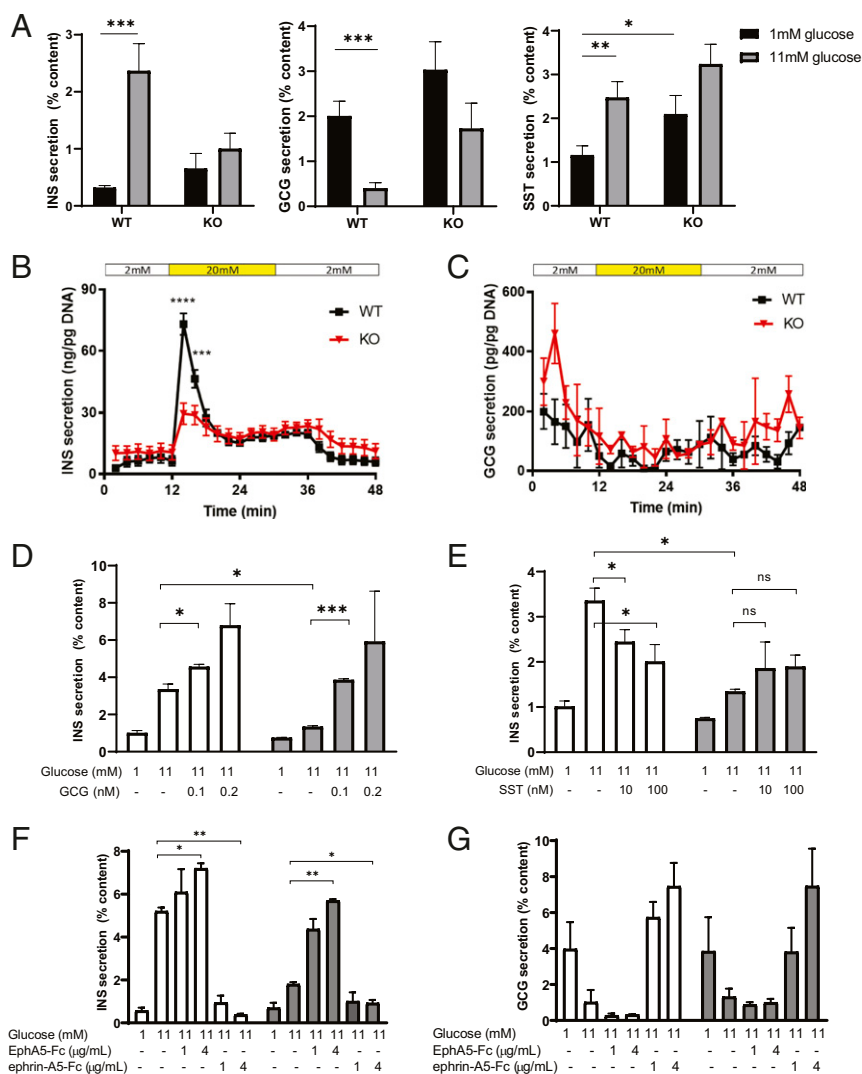


**Fig. 3.** Primary cilia mediate paracrine regulation of islet cells. (A)  $\beta$ CKO islets exhibit altered hormone secretion from  $\beta$ -,  $\alpha$ -, and  $\delta$ -cells. Glucose-stimulated insulin secretion (GSIS) is present in WT but not KO islets. Glucagon secretion by KO islets is higher at baseline but has a decreased response to glucose inhibition. Somatostatin secretion is significantly induced by high glucose in WT islets but not KO islets.  $n = 10$  groups of 10 islets. (B) Dynamic insulin secretion assay shows markedly abnormal GSIS in KO islets. Significant differences between WT and KO are seen during first-phase insulin secretion.  $n = 5$  or more groups of 50 islets per sample. (C) Dynamic glucagon secretion assay on the same samples as in B shows higher baseline glucagon and variable suppression by high glucose. (D) Both WT and  $\beta$ CKO  $\beta$ -cells respond to stimulation by exogenous glucagon (GCG) in a dose-dependent manner (WT,  $P = 0.0497$ ; KO,  $P = 0.0253$ ). GSIS is impaired in KO islets ( $P = 0.000485$ ). White bars = WT, gray bars = KO.  $n = 4$  mice per genotype; results are representative of three experiments. (E) WT but not  $\beta$ CKO  $\beta$ -cells respond to inhibition by exogenous somatostatin (SST) at 10 nM (WT,  $P = 0.0182$ ; KO,  $P = 0.297$ ) and 100 nM (WT,  $P = 0.0107$ ; KO,  $P = 0.348$ ). White bars = WT, gray bars = KO. (F)  $\beta$ CKO  $\beta$ -cells respond normally to juxtacrine modulation via Eph/ephrin-A5. At 4  $\mu$ g/mL, recombinant EphA5-Fc stimulates insulin secretion (WT,  $P = 0.0222$ ; KO,  $P = 0.00207$ ), while ephrin-A5-Fc inhibits insulin secretion (WT,  $P = 0.00278$ ; KO,  $P = 0.0403$ ). (G)  $\beta$ CKO  $\alpha$ -cells respond normally to juxtacrine Eph/ephrin modulation, in a pattern reciprocal to the  $\beta$ -cell response. EphA5-Fc inhibits while ephrin-A5-Fc augments glucagon secretion. Data did not reach statistical significance, but the trend is consistent across treatment doses. \* $P < 0.05$ , \*\* $P < 0.01$ , \*\*\* $P < 0.001$ , \*\*\*\* $P < 0.0001$ ; ns, not significant.

and instead exhibits a sustained increase in  $\text{Ca}^{2+}$  flux through the glucose response (Fig. 4 C and D). Composite data from 15 randomly selected regions of interest per genotype show that these defects are conserved regardless of cellular location within the islet (Fig. 4 E and F). When islets are pretreated with somatostatin to block the  $\beta$ -cell glucose response, KO islets are resistant to change in their reaction to sequential glucose challenge (SI Appendix, Fig. S5), suggesting altered sensitivity to paracrine cues.

#### $\beta$ CKO Mice Develop Glucose Intolerance and Diabetes without Obesity.

To determine the metabolic phenotype of  $\beta$ CKO mice, we performed body morphometrics and dynamic tests of glucose homeostasis

in vivo. At 8 wk of age,  $\beta$ CKO mice have body weight and length comparable to age- and sex-matched WT littermates, suggesting normal development (Fig. 5 A and B). Body composition analysis by MRI shows similar fat, lean mass, free water, and total body water content in KO and WT mice (SI Appendix, Fig. S2A).  $\beta$ CKO mice are protected from diet-induced obesity, as both males and females exhibit slower weight gain, smaller net weight gain, and lower total-body adiposity than WT mice over 20 wk of high-fat feeding (Fig. 5 C and SI Appendix, Fig. S2 B and C).

Despite reduced adiposity, KO mice exhibit susceptibility to diabetes. Both female and male KO mice have higher fasting blood glucose than WT mice, a difference that persisted after

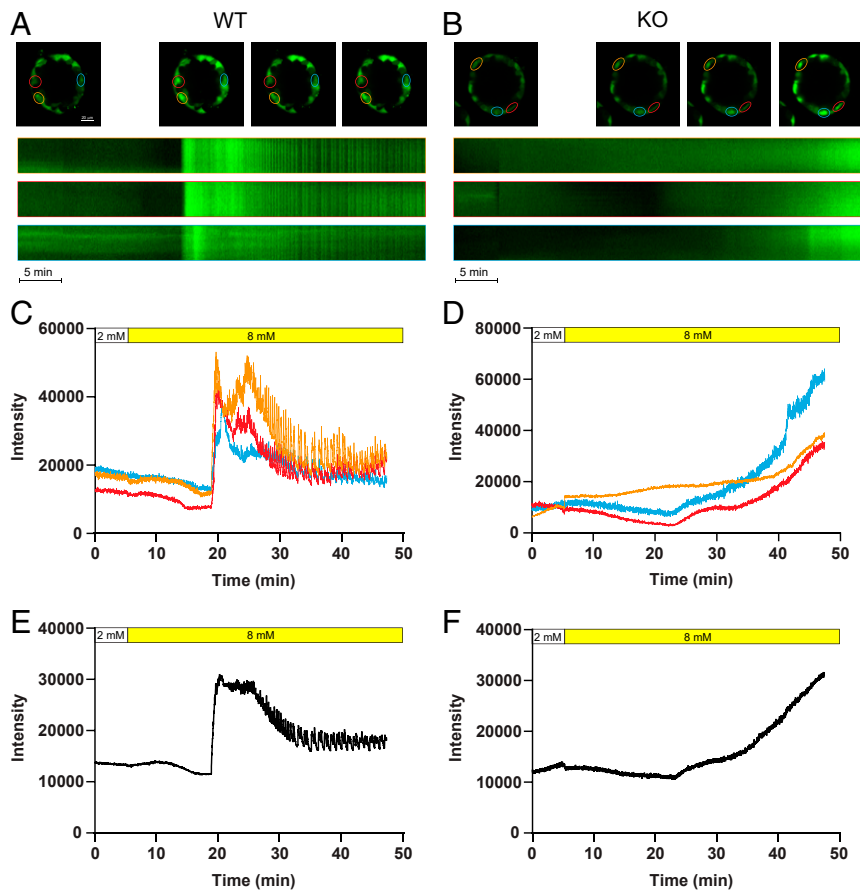


**Fig. 4.** Primary cilia regulate  $\beta$ -cell  $\text{Ca}^{2+}$  response to glucose. (A and B)  $\text{Ca}^{2+}$  responses as measured by Fluo-4 intensity and time-lapse kymographs in WT and KO islets during glucose stimulation. Three representative regions of interest are selected for analysis and are outlined in orange, red, and blue, corresponding to the color borders of kymographs and individual traces in C and D. (C and D) Single-cell traces showing aberrant  $\text{Ca}^{2+}$  glucose response in KO islet cells, which are missing both the initial burst and sustained second-phase oscillations seen in WT cells. (E and F) Integrated fluorescence intensity at the population level show that KO islets lack coordinated  $\beta$ -cell coupling and  $\text{Ca}^{2+}$  oscillations.  $n = 15$  cells per genotype. Total  $n$  examined = 121 (6 islets)  $\beta$ CKO, 148 cells (6 islets) WT.

high-fat feeding (Fig. 5D).  $\beta$ CKO mice have decreased capacity to secrete insulin in vivo (Fig. 5E), resulting in impaired glucose clearance (Fig. 5F and G). These differences are accentuated by the fact that we use the standard weight-based glucose dosing in the glucose tolerance test (GTT) (23), resulting in KO mice receiving less glucose due to lower fat mass, yet they still cannot clear it as readily as WT mice can. Insulin tolerance tests (ITTs) show no evidence of insulin resistance in KO mice on chow or high-fat diet (Fig. 5H and I), as expected due to their relatively lean body composition. Taken together,  $\beta$ CKO mice represent a model of diabetes without obesity, with a defect in glucose-dependent insulin secretion.

#### **$\beta$ CKO Mice Exhibit Abnormal Hormone Profile and Energy Metabolism.**

Since  $\beta$ CKO mice display fasting hyperglycemia and glucose intolerance, we examined their whole-body glucose dysregulation by measuring glucoregulatory parameters via circulating hormones. Tail vein blood from nonfasted mice was used to measure serum levels of insulin, glucagon, GLP-1, and leptin. Consistent with their defect in glucose-stimulated insulin secretion during GTT,  $\beta$ CKO mice have significantly lower nonfasting insulin levels than those of WT controls ( $0.35 \pm 0.064$  vs.  $0.66 \pm 0.097$  ng/mL females,  $0.67 \pm 0.12$  vs.  $1.08 \pm 0.14$  ng/mL males) (Fig. 6A, first panel). Glucagon levels vary widely in both KO and WT mice, with KO exhibiting higher means than WT ( $14.33 \pm 2.87$  vs.  $6.22 \pm 1.15$  pg/mL females,  $26.48 \pm 2.95$  vs.  $18.04 \pm 2.73$  pg/mL males)

(Fig. 6A, second panel). Both hypoinsulinemia and hyperglucagonemia likely contribute to the diabetic phenotype of  $\beta$ CKO mice. GLP-1 and leptin levels are comparable among WT and KO mice (Fig. 6A, third and fourth panels), indicating that these hormones are not responsible for the altered insulin and glucagon secretion, nor are the incretin and appetite-regulatory pathways directly involved in the development of diabetes in  $\beta$ CKO mice.

To examine the effect of  $\beta$ -cell cilia loss on systemic energy metabolism, we measured respiratory gas exchange, locomotor activity, food intake, and energy expenditure. Individual metabolic cage scans show an increased respiratory exchange ( $\text{CO}_2/\text{O}_2$ ) ratio in high-fat-fed  $\beta$ CKO mice, suggesting a preference for carbohydrate metabolism in the setting of dietary fat abundance (Fig. 6B and C). Energy expenditure in  $\beta$ CKO mice is decreased over both light and dark cycles despite normal circadian periodicity and amplitude in locomotor activity and food intake. Together these results show that adult KO mice have impaired fat metabolism, a surprising observation since both insulin deficiency and glucagon excess promote fatty acid oxidation. Animals on chow diet show less pronounced differences than on high-fat diet (SI Appendix, Fig. S4).

**Identification of  $\beta$ -Cell Cilia-Dependent Signaling Pathways.** Primary cilia modulate signaling pathways in a cell type-dependent manner, notably those downstream of Notch, Hedgehog, transforming growth factor beta (TGF- $\beta$ ), and other G protein-coupled

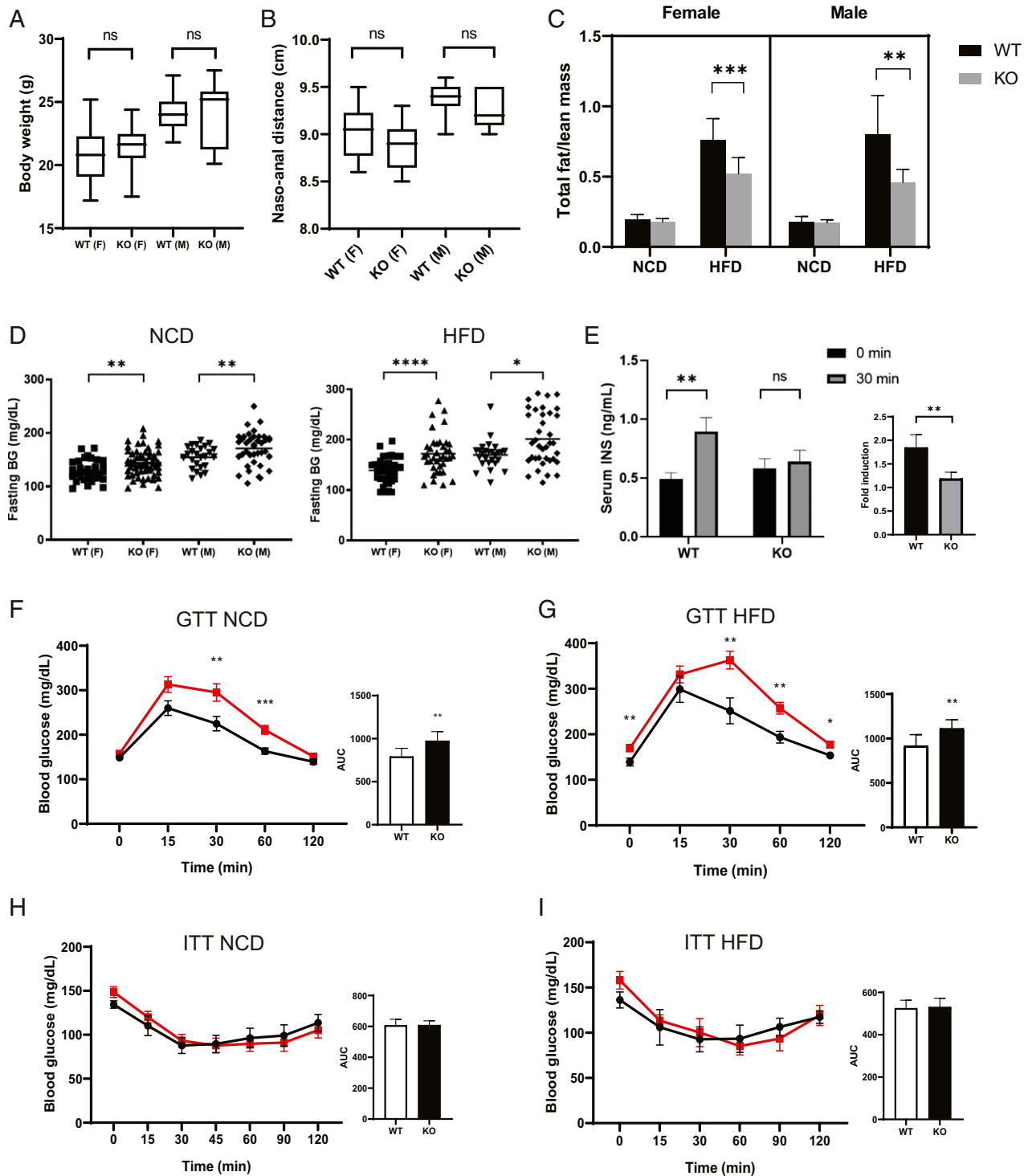


**Fig. 5.**  $\beta$ CKO mice develop glucose intolerance and diabetes without obesity. (A) Body weights at age 8 wk are comparable between WT and  $\beta$ CKO mice. (B) Body lengths as measured by naso-anal distance are comparable between WT and  $\beta$ CKO mice. (C) Body composition as measured by MRI shows resistance to diet-induced obesity in  $\beta$ CKO mice. Total fat:lean mass ratio increases in WT mice when diet changes from normal chow diet (NCD) to high-fat diet (HFD), but significantly less so in KO mice. Mean  $\pm$  SEM,  $n = 8$  to 12 mice per genotype, sex, and diet group (72 total). (D)  $\beta$ CKO mice at 8 to 12 wk of age on chow diet have significantly higher fasting blood glucose levels than WT mice (females,  $P = 0.0017$ ; males,  $P = 0.0096$ ). This difference persists after administration of high-fat diet (females,  $P < 0.0001$ ; males,  $P = 0.0305$ ). (E) Insulin induction at 30 min after intraperitoneal glucose challenge (2 g/kg) in female mice ( $n = 18$  WT, 27 KO). WT mice have significant increase in serum insulin.  $P = 0.00256$ . KO mice fail to secrete insulin in response to glucose. Fold induction is 2.02 WT, 1.16 KO.  $P = 0.0048$ . (F) GTT in female mice on normal chow diet. KO mice have impaired glucose clearance at 30 min ( $P = 0.00733$ ) and 60 min ( $P = 0.000184$ ) following intraperitoneal glucose administration (2 g/kg);  $n = 35$  WT, 33 KO. The area under the curve (AUC) is higher for KO mice ( $P = 0.0016$ ). (G) GTT in female mice after 8 wk of high-fat diet. KO mice had higher glucose levels at 0 min ( $P = 0.0095$ ), 30 min ( $P = 0.00212$ ), 60 min ( $P = 0.00129$ ), and 120 min ( $P = 0.0172$ ) following glucose administration.  $n = 23$  WT, 21 KO. AUC is higher in KO mice ( $P = 0.0072$ ). (H) Insulin tolerance test on 4-h fasted female mice on chow diet ( $n = 8$ ). (I) Insulin tolerance test on 4-h fasted female mice on high-fat diet ( $n = 8$ ). \* $P < 0.05$ , \*\* $P < 0.01$ , \*\*\* $P < 0.001$ , \*\*\*\* $P < 0.0001$ ; ns, not significant.

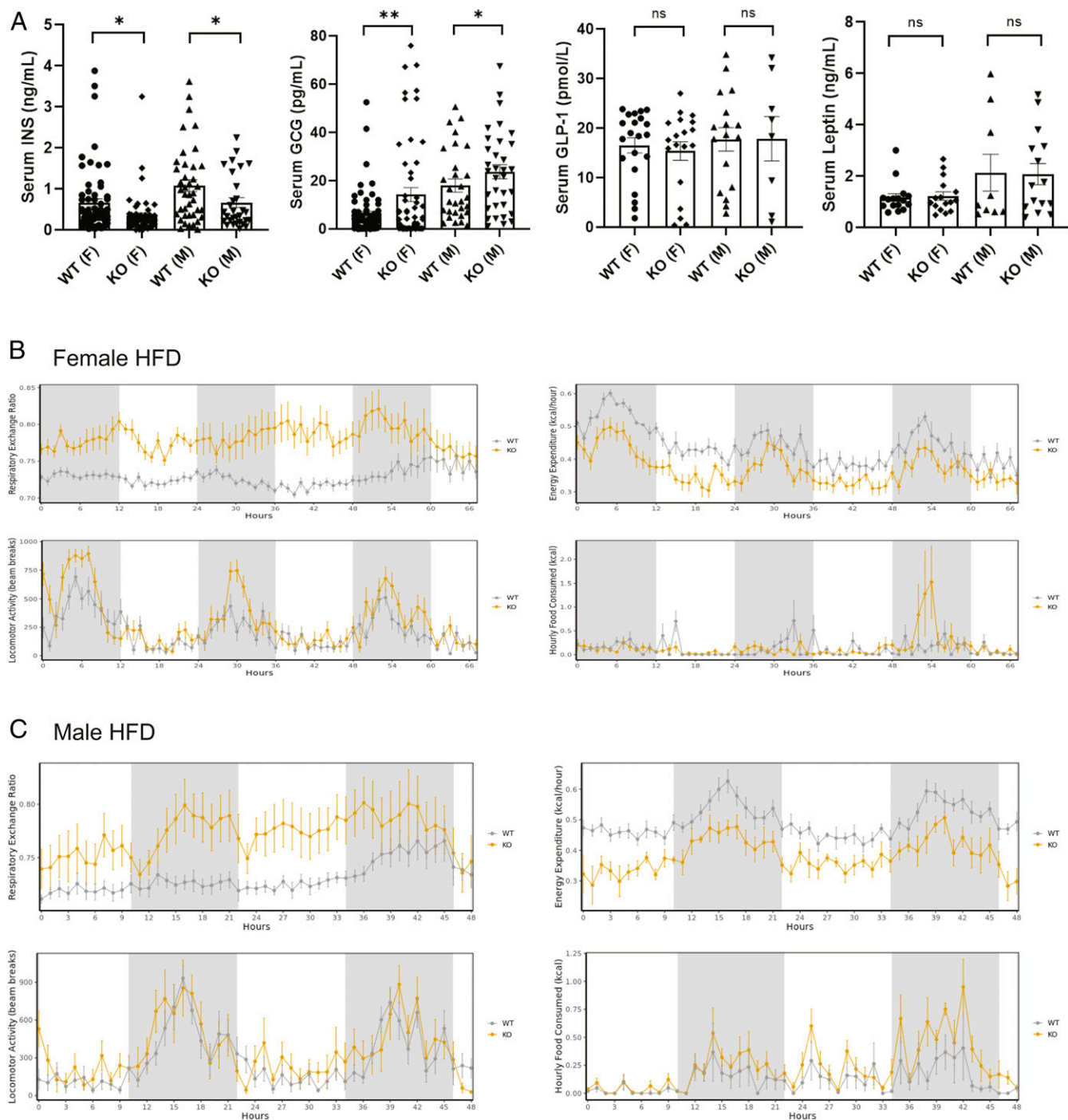


**Fig. 6.**  $\beta$ CKO mice exhibit abnormal hormone profile and energy metabolism. (A) Circulating nonfasting hormone levels in age-matched WT and KO mice. KO mice have significantly lower serum insulin than WT mice (female,  $P = 0.0114$ ; male,  $P = 0.039$ ) and higher glucagon (female,  $P = 0.0064$ ; male,  $P = 0.0443$ ). GLP-1 and leptin are not significantly different between WT and KO mice. (B) KO female mice on a high-fat diet exhibit an increased respiratory exchange ratio and decreased energy expenditure in calorimetry studies. Locomotor activity and food intake are not significantly different between KO and WT. (C) Similar findings in KO male mice on a high-fat diet. In both male and female cohorts,  $n = 4$  mice per genotype; data are representative of three independent experiments, and total number examined = 72 mice. \* $P < 0.05$ , \*\* $P < 0.01$ ; ns, not significant.

receptors (24–27). To identify cilia-dependent signaling pathways in pancreatic islets, we conducted an unbiased profiling of protein expression and phosphorylation changes associated with  $\beta$ -cell cilia deletion. Using a phosphoprotein array consisting of 1,318 paired protein-specific and phosphospecific antibodies and a signaling protein array with 1,358 antibodies (28, 29), we identified over 100 differentially expressed ( $P < 0.05$ ) proteins and potential

substrates and effectors that participate in cilia-dependent signaling (SI Appendix, Fig. S6A). After the proteome and phosphoproteome datasets were ordered by the lowest  $P$  value, lowest false discovery rate (FDR), and highest fold change (FC), gene ontology analysis showed enrichment in proteins controlling cell communication, GPCR signaling, TGF signaling, the cell cycle, and apoptosis, among other pathways (SI Appendix, Fig. S6B).

We examined several groups of proteins in detail, each corresponding to functional defects observed in  $\beta$ CKO islets. Intraislet levels of insulin, glucagon, and somatostatin differ among  $\beta$ CKO and WT islets (*SI Appendix, Fig. S6C, Left*). The cullin E3 ligase family controls intraislet paracrine signaling via somatostatin (30) and is elevated in KO islets, consistent with abnormally high somatostatin seen in both the secretion assay and protein array (*Fig. 3A and SI Appendix, Fig. S6C*). We observe concomitant changes in paracrine factors inducible nitric oxide synthase and endothelial nitric oxide synthase which are typically released from islet monocytes or the endothelium in the setting of islet stress (31–33). The vascular remodeling regulator VEGFR2 and its Tyr-1175 phosphorylation are decreased in  $\beta$ CKO islets, which may indicate reduced ability to support vascular function (34, 35). There are lower steady-state levels of TGF $\beta$ 2, its signaling effector Smad3, and  $\beta$ -catenin, which regulate insulin secretion in addition to other roles in  $\beta$ -cell function (36–39). Synuclein A inhibits insulin secretion by binding to  $K_{ATP}$  channels and secretory granules (40), while PDGFR is a cilia-dependent microtubule modulator (27, 41), and both are increased in  $\beta$ CKO islets.

Loss of cilia resulted in altered cytoskeletal remodeling and cell–cell connectivity (*SI Appendix, Fig. S6C, Middle*), including levels of focal adhesion proteins integrin  $\beta$ 1 and E-cadherin, along with tight junction proteins (claudins), desmosomes (desmin), intraislet lamin A, and collagen. Together, these can impart profound changes in islet cell adhesion, permeability, and electrochemical coupling (42–46). Potassium channels are critical conduits of  $\beta$ -cell electrical activity (47, 48), and  $\beta$ CKO islets exhibit altered levels of voltage-gated  $K^+$  channels Kv1.1, Kv1.3, Kv3.2, inward rectifying Kir2.1, and KCNK4, consistent with their defect in insulin secretion (*SI Appendix, Fig. S6B, Right*). While the protein arrays did not probe for voltage-gated calcium channel subunits, several key calcium-sensitive signaling pathways are detected as altered in  $\beta$ CKO islets. ER stress markers calreticulin and calnexin are elevated, while CaMK and calmodulin, the binding partner of cilia centrioles and acute  $Ca^{2+}$  sensors for vesicle exocytosis (49, 50), were among the most severely down-regulated factors (*SI Appendix, Fig. S6C, Right*). Collectively, these coordinated changes in ion channel and calcium signaling are consistent with reduced  $\beta$ -cell excitation and secretory function in the absence of primary cilia.

## Discussion

Recent work has explored the link between ciliary dysfunction and diabetes (10, 11, 15, 51). Here we show that primary cilia are

required for multiple aspects of  $\beta$ -cell function, and we globally survey the cilia-dependent signaling network in islets. Our findings suggest that  $\beta$ -cell primary cilia are required not only for glucose-mediated insulin secretion but also for reciprocal regulation with  $\alpha$ - and  $\delta$ -cells, pointing to an integrated role of primary cilia in islet cell cross talk and in the regulation of glucose homeostasis (*Fig. 7*).

Our study shows that primary cilia are present on the surface of normal mouse and human  $\beta$ -cells (*Fig. 1 and SI Appendix, Fig. S1*), where they orchestrate a network of intracellular and intercellular events. Through targeted disruption of  $\beta$ -cell primary cilia, the  $\beta$ CKO mouse gives a specific view of the role of  $\beta$ -cell cilia in diabetogenesis, which offers more mechanistic insight than can be gleaned from the complex metabolic phenotypes of whole-body cilia deficiency (11, 12, 52). In agreement with the recent report of an inducible Pdx1-Cre cilia knockout mouse (15), deletion of  $\beta$ -cell cilia in our model reduces  $\beta$ -cell secretory function, which causes a state of relative insulin insufficiency, glucose intolerance, and diabetes (*Figs. 2, 3, and 5*). Our  $\beta$ CKO mouse phenocopies human diabetes in its hypoinsulinemia, hyperglucagonemia, and abnormal glycemic state (*Figs. 5–6*). Given the relatively mild nature of hyperglycemia, the changes in  $\beta$ -cell phenotype in our model is likely not a secondary effect of glucotoxicity (53–55) but rather results from disrupted cilia function and the abnormal glucose-sensing and paracrine dysregulation that ensue.

The second major finding from this study is that the  $\beta$ -cell cilium functions beyond the regulation of  $\beta$ -cell intrinsic activities. Intercellular connectivity and feedback regulation among islet  $\alpha$ -,  $\beta$ -, and  $\delta$ -cells underlies the functionality of the islet as a unit, while loss of connectivity is a feature of both type 1 and type 2 diabetes (3, 21, 56). Our data demonstrate a critical role for primary cilia in cellular cross talk within the islet environment (*Figs. 3 and 4 and SI Appendix, Fig. S5*). We show that the  $\beta$ -cell response to somatostatin is critically dependent on the cilia, consistent with the observation that the somatostatin receptor SSTR3 localizes to  $\beta$ -cell cilia while other SSTR isoforms may be nonciliary (57–59). The exact subtype of somatostatin receptor responsible for transmitting cilia-dependent  $\delta$ - to  $\beta$ -cell signals remains to be determined. There has been no report to date of glucagon receptor localization to cilia in any cell type, consistent with our observation that the  $\beta$ -cell response to exogenous glucagon was unaffected by the absence of cilia (*Fig. 3D*).

As islet topology dictates close proximity between the  $\alpha$ -,  $\beta$ -, and  $\delta$ -cell bodies and their cilia (4) and because the cilium represents a nexus for GPCR and other receptor signaling, we

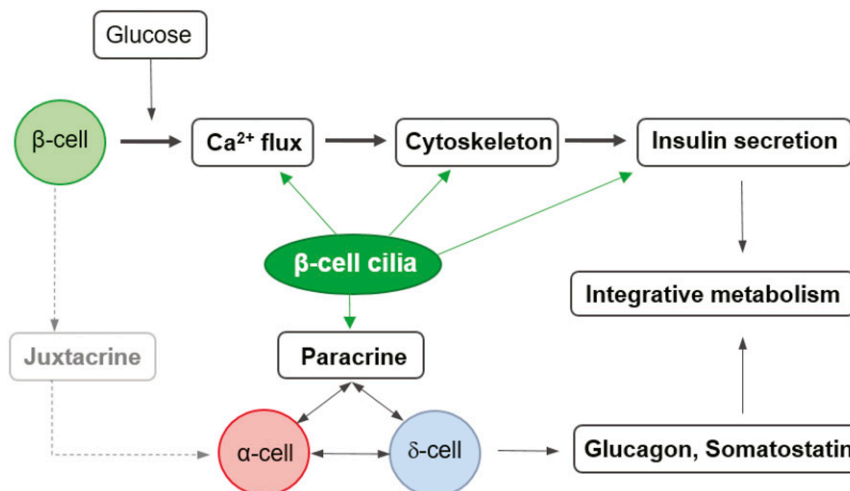


**Fig. 7.** Cilia-dependent signaling pathways in the  $\beta$ -cell. Schematic of primary cilia actions in the islet, including modulation of  $\beta$ -cell-intrinsic functions and paracrine regulation of  $\alpha$ - and  $\delta$ -cells to produce a coordinated effect on integrative metabolism.



hypothesized that cilia may transduce multiple types of signals between neighboring islet cells. Our findings show that the main signal is paracrine in nature and that the lost reciprocal regulation among  $\alpha$ -,  $\beta$ -, and  $\delta$ -cells via their secreted hormones results in an inability for the islet to function as a unit. Primary cilia in human islets likely play an even more prominent role as a cross talk regulator, given the increased heterogeneity and intermingling of  $\alpha$ -,  $\beta$ -, and  $\delta$ -cells in the human islet (60, 61). As for other modes of cellular cross talk, others have identified physical cellular extensions on  $\delta$ -cells that give a structural basis for intraislet communication (62), as well as cilia-dependent phosphorylation of Eph/ephrin signaling components (15). In our studies, we find  $\beta$ CKO islets to have slightly reduced protein levels of select ephrin family members A7 and B2 [array datasets GSE138885 (29) and GSE138856 (28)], while other ephrins were not included in the array. Functionally, both  $\alpha$ - and  $\beta$ -cells in  $\beta$ CKO islets have normal responses to Eph/ephrin-A5 modulation (Fig. 3 F and G), suggesting that ephrin-mediated juxtacrine signals control hormone secretion independent of cilia. Thus, we favor a model where juxtacrine signaling occurs in parallel to cilia-regulated paracrine signaling in islet cells.

Glucose stimulates  $\text{Ca}^{2+}$  influx and oscillations in the  $\beta$ -cell, a process that we show to be cilia dependent. Our functional imaging studies reveal that cilia-deficient  $\beta$ -cells exhibit abnormal  $\text{Ca}^{2+}$  entry and total abolishment of  $\text{Ca}^{2+}$  oscillations, which offers a mechanistic explanation for severely impaired insulin secretion (Figs. 3–4 and *SI Appendix, Fig. S5*). The molecular basis underlying cellular  $\text{Ca}^{2+}$  regulation by cilia remains to be elucidated. One possibility would be that  $\beta$ -cells possess  $\text{Ca}^{2+}$  channels on their ciliary membrane (63) and that ciliary  $\text{Ca}^{2+}$  fluxes serve as gatekeepers of cytosolic  $\text{Ca}^{2+}$ . Alternately, the cilia may relay signals from ambient stimuli to open  $\text{Ca}^{2+}$  channels on the plasma membrane (64, 65). It would be prudent to test these scenarios in both mouse and human  $\beta$ -cells, as there exist considerable differences in their  $\text{Ca}^{2+}$  channel expression, distribution, and activation (66).

A question that remains unanswered is how  $\beta$ -cell cilia modulate whole-body energy metabolism. Our calorimetry studies suggest that  $\beta$ -cell cilia are important for systemic energy expenditure and fuel usage.  $\beta$ CKO mice have reduced body weight and adiposity, and metabolic differences between WT and KO mice intensified when animals were challenged with high-fat diet, suggesting that KO mice had a reduced ability to use fat as a fuel source even when it is available in excess (Figs. 5–6 and *SI Appendix, Fig. S3 and S4*). Of note, the combination of impaired fasting glucose and impaired glucose tolerance without obesity and insulin resistance distinguishes our mouse model from classic type 2 diabetes (67). What is not yet known is how other metabolic tissues in  $\beta$ CKO mice contributed to their calorimetry phenotype in the setting of altered circulating insulin and glucagon and what islet products other than insulin and glucagon might be influencing metabolism.

Primary cilia control cellular homeostasis by regulating protein stability (68). Our proteomic and phosphoproteomic profiling classifies cilia-dependent signaling pathways in islets by functional protein groups. We observed global changes in cellular proteostasis and specific modulation of pathways governing paracrine signaling, hormone secretion, islet cell connectivity, and calcium activation, corresponding to the main deficits identified in  $\beta$ CKO islets (*SI Appendix, Fig. S6*). In addition to these functional clusters, our datasets reveal perturbations in key cellular mechanisms, including the ubiquitin–proteasome system, mTOR and PI3K/AKT signaling, and the cell cycle. There is increasing evidence that these processes exhibit reciprocal regulation onto ciliogenesis itself (69, 70), thus representing a feedback mechanism in cilia formation and maintenance. While these additional pathways were not individually validated by functional experiments in this study, they should be the target of future investigations.

## Methods

**Materials.** All antibodies, chemicals, kits, primers, probes, and software are listed in the *SI Appendix, Key Resources Table*.

**Mice.** Ins1-Cre and Ins1-CreERT2 mice from Jackson Laboratories (JAX #026801, #026802) were crossed to *Irf8<sup>fl/fl</sup>* mice (JAX #022409). Wild-type C57BL/6J (JAX #000664) were used as a control along with *Cre<sup>-/-</sup>* or *Flox<sup>-/-</sup>* littermates. Mice were genotyped at weaning by a commercial vendor (Transnetyx). Mice were fed a standard rodent diet (PicoLab Mouse Diet 5053, 13.2% calories from fat) or a moderately high fat diet (PicoLab Mouse Diet 5058, 21.6% calories from fat) as specified. Mice were used at 2 to 4 mo of age for secretion and calcium experiments and between 2 and 12 mo of age for glucose tolerance and physiology studies. To induce Cre recombination,  $\beta$ CKO-ERT2 mice were injected daily for 5 d with tamoxifen (50  $\mu\text{g/g}$  body weight) or corn oil as vehicle control. Animals were maintained in accordance with Institutional Animal Care and Use Committee regulations at the Washington University School of Medicine.

**Islet Isolation and Culture.** Islets were isolated from young adult mice at 2 to 4 mo of age using collagenase digestion with a modified Lacy protocol (71, 72). Typical yield is 100 to 150 islets per mouse. Isolated islets were recovered overnight prior to experiments in a 37 °C, 5%  $\text{CO}_2$  incubator in 10-cm plates with 15 mL islet media/plate (RPMI 1640 with 10% fetal bovine serum [FBS], penicillin–streptomycin, and 11 mmol/L glucose). Ex vivo Cre induction was performed in isolated  $\beta$ CKO-ERT2 islets using 2.5  $\mu\text{mol/L}$  of 4-hydroxy tamoxifen (Santa Cruz sc-3542) in the culture media and replenished with media change every 2 d. Loss of cilia was confirmed by immunostaining and functional assays within 96 h of tamoxifen treatment. Human islets were obtained via the Integrated Islet Distribution Program from deceased donors. Upon arrival, human islets were cultured overnight in islet media prior to experimentation.

**Islet Live-Cell Sorting by Flow Cytometry.** Isolated islets were dispersed by incubating in Accutase (Innovative Cell Tech, Cat #AT-104) at 37 °C for 2  $\times$  5 min and washed with Hanks' Balanced Salt Solution (HBSS) buffer without  $\text{Ca}^{2+}$  and  $\text{Mg}^{2+}$ . Dispersed islets were incubated in RPMI supplemented with 10% FBS and 1  $\mu\text{M}$  FluoZin-3 (ThermoFisher F24195) at 37 °C for 20 min to label  $\beta$ -cells. Islet cells were washed in fluorescence-activated cell sorting (FACS) buffer (HBSS with 2% FBS), filtered through a 40  $\mu\text{m}$  strainer, and resuspended in FACS buffer at  $1 \times 10^6$  cells/mL. Cells were sorted on a FACSAria-II and gated as GFP-positive  $\beta$ -cells or GFP-negative non- $\beta$ -cells. FSC:SSC-W gating was used to exclude cell doublets (<10%) from analysis or collection.

**Immunohistochemistry.** Isolated islets were washed with PBS and fixed with 4% paraformaldehyde (PFA) for 15 min and permeabilized with 0.3% Triton X-100 in PBS (PBST) for 10 min at room temperature. After incubation with blocking buffer PBS with 10% normal goat serum for 1 h at room temperature, islets were incubated overnight at 4 °C with primary antibodies diluted in PBST. The next day, islets were washed, incubated with secondary antibodies for 1 h at room temperature, and washed again in PBST. DAPI provided nuclear counterstain. Islets were mounted on glass slides with Prolong Gold Anti-fade (Thermo Fisher P36930). Pancreas sections were either flash frozen in optimal cutting temperature (OCT) compound and cut into cryosections or fixed in zinc formalin (Z-Fix, Thermo Fisher NC9351419) or 4% PFA (Electron Microscopy Sciences 15710), dehydrated in 10 to 30% sucrose, and prepared as paraffin or frozen sections. OCT sections were fixed in methanol and stained using the above methods. All islet and OCT sections were imaged using an inverted Zeiss LSM880 fluorescence microscope (Nikon, Ti-E).

**Islet Composition Analysis.** Paraffin-embedded or 4% PFA-fixed pancreas sections with 6 to 15  $\mu\text{m}$  thickness were deparaffinized using xylene and rehydrated with graded alcohol or PBS, respectively. Antigen retrieval was performed by heating samples in sodium citrate solution (pH 6.0) for 30 min followed by permeabilizing in 0.1% Triton X and blocking in 2% bovine serum albumin (BSA) for 1 h. Antibodies used for staining are detailed in *SI Appendix, Key Resources Table*. Quantification of cellular composition, including islet size, diameter, and  $\beta$ -,  $\alpha$ -, and  $\delta$ -cell mass as defined by glucagon, insulin, and somatostatin-positive signals per islet area, was performed in ImageJ. Islet contour was manually traced based on the boundaries of hormone staining, and the number of pixels within the region of interest was quantified as total islet area. Circularity scores were calculated using the following formula: circularity =  $4\pi(\text{area}/\text{perimeter}^2)$ , where a value of 1.0

indicates a perfect circle. In total, we analyzed over 200 whole-pancreatic sections from six to eight age-matched animals per genotype. Islet composition was analyzed independently by two researchers who were blinded to the genotype, and results were cross validated.

**Quantitative PCR.** Isolated mouse islets were lysed in 350  $\mu$ L of RLT lysis buffer supplemented with  $\beta$ -mercaptoethanol per 100 islets. RNA was purified with a Qiagen RNeasy mini kit, and cDNA was synthesized using a Thermo Fisher High-Capacity cDNA reverse transcription kit at 200 ng/20  $\mu$ L. qPCR was performed in duplicate on a 7900 Step One Plus RT-PCR machine (Applied Biosystems) using 2 $\times$  TaqMan Mastermix (Thermo Fisher 4324018) and 20 $\times$  TaqMan Gene Expression assay for the IFT88 gene (Thermo Fisher 4331182). Changes in gene expression were quantified using  $2^{-\Delta\Delta CT}$ , and results were normalized to the housekeeping gene RPL32.

**Western Blot.** Mouse islets were isolated and stored at  $-80^{\circ}\text{C}$  until lysis. Using a minimum of 80 islets per sample, islets were sonicated in 30  $\mu$ L lysis buffer (Cell Signaling Technology) containing cOMplete mini protease inhibitor mixture (Roche) and lysed on ice for 30 min. Protein concentration was determined by BCA Protein Assay (Thermo Fisher). Lysates were prepared as 15  $\mu$ g protein/30  $\mu$ L and denatured at  $70^{\circ}\text{C}$  for 10 min. Samples were run on a Mini-Protein 4 to 20% precast gel (BioRad) and transferred to a nitrocellulose membrane. Blots were incubated overnight with the primary antibodies anti- $\beta$ -actin (Abcam ab8226, 1:1,000) and anti-IFT88 (Proteintech 13967-1-AP, 1:1,000). Signal was detected using fluorescent dye-labeled secondary antibodies (1:10,000). Fluorescence intensity was quantified with Image Studio Lite (Li-Cor).

**Static Secretion Assay.** Islets were equilibrated in Krebs-Ringer bicarbonate Hepes (KRBH) buffer (128.8 mmol/L NaCl, 4.8 mmol/L KCl, 1.2 mmol/L  $\text{KH}_2\text{PO}_4$ , 1.2 mmol/L  $\text{MgSO}_4\cdot 7\text{H}_2\text{O}$ , 2.5 mmol/L  $\text{CaCl}_2$ , 20 mmol/L Hepes, 5 mmol/L  $\text{NaHCO}_3$ , and 0.1% BSA [pH 7.4]) at 2.8 mmol/L glucose for 45 min at  $37^{\circ}\text{C}$ . Islets were then transitioned to 1 or 11 mmol/L glucose for 1 h at  $37^{\circ}\text{C}$  in groups of 10 to 20 islets per tube. In select experiments (Fig. 3 D–G), islets were cotreated with glucagon, somatostatin, or recombinant ephrin-A5-Fc or EphA5-Fc (R&D Systems) during glucose stimulation. Supernatant was collected after 1 h, and islet hormone content was extracted overnight in acid-ethanol (1.5% 12 N HCl in 70% ethanol). Insulin, glucagon, and somatostatin concentrations were measured by enzyme-linked immunosorbent assay (ELISA), and secretion data were presented as a percentage of hormone content.

**Dynamic Secretion Assay.** The perfusion system was assembled as reported previously (39). Isolated islets were assayed with effluent collected at a 100  $\mu$ L/min flow rate every 2 min over sequential glucose changes (2, 20, 2 mM). After sample collection, DNA was quantified using the PicoGreen assay (Life Technologies, P7589), and insulin and glucagon in the effluent were measured by ELISA.

**ELISA.** Insulin, glucagon, GLP-1, and leptin ELISA kits were obtained from Crystal Chem (#90080, #81518, #81508, #90030). The somatostatin ELISA kit was obtained from Phoenix Pharmaceuticals (EK-060-03). Mouse whole blood was collected via tail tip, and serum was isolated after clotting by centrifuging at 10,000 rpm for 10 min. Between 5 and 20  $\mu$ L of serum or secretion sample were used for ELISA per the manufacturer's protocol. Each sample was assayed in triplicate.

**Glucose and Insulin Tolerance Test.** Mice were fasted for 6 h before receiving intraperitoneal injection of 2 g/kg body weight of sterile glucose solution (GTT) or fasted for 4 h before receiving 0.5 unit/kg body weight of human recombinant insulin (ITT, HI-213 Lilly). Blood glucose was measured on tail vein blood at preinjection (0 min) and 15, 30, 60, 90, and 120 min after glucose or insulin injection. For serum insulin measurements, blood was taken pre- and postinjection (0 and 30 min), clotted, and centrifuged at 10,000 rpm for 10 min, and serum was assayed for insulin concentration using ELISA.

**Body Composition and Metabolic Phenotyping.** Comprehensive metabolic, behavioral, and physiological variables were determined by TSE/PhenoMaster at the Washington University Diabetes Models Phenotyping Core. Body composition was analyzed using EchoMRI (Echo Medical Systems) for measuring the percentage body fat and lean mass in awake animals. For metabolic phenotyping, mice were fed a chow diet or high-fat diet for 20 wk. Animals were acclimated to the core facility for 1 wk prior to experimentation,

then for an additional 24 h in individual metabolic cages prior to data collection. Parameters measured include oxygen ( $\text{O}_2$ ) consumption, carbon dioxide ( $\text{CO}_2$ ) production, energy expenditure, locomotor activity, and food and water intake. The respiratory exchange ratio (RER) was calculated as the ratio of  $\text{CO}_2$  production to  $\text{O}_2$  consumption:  $\text{RER} = \text{VCO}_2/\text{VO}_2$ . Data were analyzed by *CaIR* using a general linear model modified from analysis of covariance (ANCOVA) and ANOVA by accounting for mass effects in calorimetry studies (73, 74).

**Live-Cell Calcium Imaging.** Islets were incubated with 4  $\mu$ M of Fluo4-AM for 45 min at  $37^{\circ}\text{C}$ , 5%  $\text{CO}_2$  in KRBH buffer (pH 7.4, 0.1% BSA) containing 2 mM glucose. Islets were equilibrated for 5 min in a climate-controlled microscope stage at  $37^{\circ}\text{C}$ , 5%  $\text{CO}_2$ . All imaging experiments were performed with glucose concentrations at a steady state. All experiments took place in 2 mL buffer volume using MatTek glass bottom microwell dishes No. 1.5 (0.16 to 0.19 mm). In select experiments (*SI Appendix, Fig. S5*), islets were preincubated with 100 nM somatostatin for 1 h prior to Fluo-4 labeling. Results were representative of five independent experiments; islets from both male and female mice were examined. Confocal imaging was conducted using a Zeiss 880 microscope on Fluo4-AM-labeled islets with 488 nm laser excitation, and emission was detected at 500 to 570 nm using a spectral detector. Images were captured using a Zeiss Plan-Apochromat 63 $\times$  1.4 oil immersion differential interference contrast objective and acquired at a frame size of  $512 \times 512$  ( $135 \times 135 \mu\text{m}^2$ ) with a pixel dwell time of 2.06  $\mu$ s, resulting in a frame time of 0.633 s. The pinhole size was kept at 206.6  $\mu$ m to allow for sufficient signal-to-noise ratio. Baseline time series images at 2 mM glucose were acquired for 320 s. Glucose concentration was then increased to 8 mM by manual pipetting. After glucose addition, the islet position and imaging plane were checked and adjusted if necessary. Islets were allowed to equilibrate for another 2 min, followed by multiple imaging series of 320-s cycles. Image series were concatenated, drift was corrected by the Nano J-Core ImageJ plugin (75), and intensity profiles and kymographs were generated for quantification.

**Transmission Electron Microscopy.** Islet ultrastructure was assessed with electron microscopy. Isolated islets are fixed in Karnovsky's solution (3% glutaraldehyde, 1% paraformaldehyde), followed by a secondary fixation in osmium tetroxide, dehydrated in alcohol, embedded in resin, and polymerized at  $90^{\circ}\text{C}$  for 48 h. Ultrathin sections of 90 nm thickness were cut and stained with uranyl acetate and examined with a JEOL 1200 EX.

**Protein Expression Arrays.** The Phospho Explorer Antibody Array (PEX100) and Signaling Explorer Antibody array (SET100) were manufactured by Full Moon Biosystems. Two groups of two  $\beta$ CKO and two untreated  $\beta$ CKO-ERT2 (WT) control male mice aged 8 to 10 wk were used as experimental replicates. Total protein was extracted from  $\beta$ CKO and control islet lysates, labeled with biotin, conjugated to preblocked microarray slides, and detected with Cy3-streptavidin. Slides were returned to Full Moon BioSystems for scanning. Spot intensities were extracted from the scanned array images using GenePix 5. Background readings from each array were subtracted for each spot, and average median signal was used for analysis. The array was normalized against total average spot intensity on the array.

**Bioinformatics.** Differential expression between samples was calculated by dividing the expression ratio of KO by WT. Proteins with expression fold change of  $>1.5$  or  $<0.5$  between KO and WT were selected and classified for functionality using the Gene Ontology database. Those with the lowest FDR, highest FC, and known role in islet or  $\beta$ -cell regulation were curated into three functional groups. Heat maps of differentially expressed proteins ( $P < 0.05$ ) from both arrays were generated via the open resource app Heat-mapper (76), and gene enrichment analysis was done by Enrichr (77).

**Statistics.** Data are presented as mean  $\pm$  SEM. Differences between groups were compared using *t* test (two groups) or ANOVA ( $>$ two groups). PhenoMaster data were analyzed by *CaIR* using a general linear model based on ANCOVA. Sample size and number of replicates for each experiment are indicated in figure legends. Significant differences among groups with  $*P < 0.05$ ,  $**P < 0.01$ ,  $***P < 0.001$ , and  $****P < 0.0001$  are indicated.

**Data Availability.** Any data and materials that can be shared will be released via a Materials Transfer Agreement. The phosphoprotein and signaling array data have been deposited in the Gene Expression Omnibus under accession numbers GSE138856 and GSE138885.

**ACKNOWLEDGMENTS.** We thank the Millman and Remedi labs for equipment sharing, M. Hughes and Q. Zhang for bioinformatics consultation, M. Revilla and L. Peng for islet composition analysis, W. Chung for recombinant EphA2/ephrin-Fc, and A. Ustione for imaging expertise. We thank the Washington University cilia research community and C. Semenovich for critical data review. Metabolic phenotyping was performed at the Washington University Diabetes Research Center (DRC) (NIH Grant P30 DK 020579). Pancreas sections were prepared at the Washington University Musculoskeletal Core (NIH Grant P30 AR074992). Electron microscopy was performed at the DRC (NIH Grant P60 DK

020579). Light microscopy was performed at the Washington University Center for Cellular Imaging, supported by the Washington University School of Medicine, the Children's Discovery Institute of Washington University and St. Louis Children's Hospital (Grant CDI-CORE-2019-813), and the Foundation for Barnes-Jewish Hospital (3770 and 4642). This work was supported in part by the NIH (Grants DK115795A to J.W.H., DK112921 and DK020579 to F.U., F30DK111070 to D.A., and DK115972 to D.V.P.), the Endocrine Fellows Foundation (early career grant to J.W.H.), and the Doris Duke Charitable Foundation (Doris Duke Fund to Retain Clinical Scientists [DDFRCS] to J.W.H.).

1. P. E. MacDonald, P. Rorsman, Oscillations, intercellular coupling, and insulin secretion in pancreatic  $\beta$  cells. *PLoS Biol.* **4**, e49 (2006).
2. A. D. Elliott, A. Ustione, D. W. Piston, Somatostatin and insulin mediate glucose-inhibited glucagon secretion in the pancreatic  $\alpha$ -cell by lowering cAMP. *Am. J. Physiol. Endocrinol. Metab.* **308**, E130–E143 (2015).
3. R. Rodriguez-Diaz *et al.*, Paracrine interactions within the pancreatic islet determine the glycemic set point. *Cell Metab.* **27**, 549–558.e4 (2018).
4. W. J. Gan *et al.*, Cell polarity defines three distinct domains in pancreatic  $\beta$ -cells. *J. Cell Sci.* **130**, 143–151 (2017).
5. M. Yamamoto, K. Kataoka, Electron microscopic observation of the primary cilium in the pancreatic islets. *Arch. Histol. Jpn.* **49**, 449–457 (1986).
6. G. J. Pazour *et al.*, Chlamydomonas IFT88 and its mouse homologue, polycystic kidney disease gene Tg737, are required for assembly of cilia and flagella. *J. Cell Biol.* **151**, 709–718 (2000).
7. B. K. Yoder *et al.*, Polaris, a protein disrupted in orpk mutant mice, is required for assembly of renal cilium. *Am. J. Physiol. Renal Physiol.* **282**, F541–F552 (2002).
8. J. H. Moyer *et al.*, Candidate gene associated with a mutation causing recessive polycystic kidney disease in mice. *Science* **264**, 1329–1333 (1994).
9. J. J. Schrick *et al.*, Characterization of the human homologue of the mouse Tg737 candidate polycystic kidney disease gene. *Hum. Mol. Genet.* **4**, 559–567 (1995).
10. J. M. Gerdes *et al.*, Ciliary dysfunction impairs beta-cell insulin secretion and promotes development of type 2 diabetes in rodents. *Nat. Commun.* **5**, 5308 (2014).
11. S. Mujahid *et al.*, The endocrine and metabolic characteristics of a large Bardet-Biedl syndrome clinic population. *J. Clin. Endocrinol. Metab.* **103**, 1834–1841 (2018).
12. G. B. Collin *et al.*, Mutations in ALMS1 cause obesity, type 2 diabetes and neurosensory degeneration in Alström syndrome. *Nat. Genet.* **31**, 74–78 (2002).
13. D. A. Cano, S. Sekine, M. Hebrok, Primary cilia deletion in pancreatic epithelial cells results in cyst formation and pancreatitis. *Gastroenterology* **131**, 1856–1869 (2006).
14. Q. Zhang, J. R. Davenport, M. J. Croyle, C. J. Haycraft, B. K. Yoder, Disruption of IFT results in both exocrine and endocrine abnormalities in the pancreas of Tg737(orpk) mutant mice. *Lab. Invest.* **85**, 45–64 (2005).
15. F. Volta *et al.*, Glucose homeostasis is regulated by pancreatic  $\beta$ -cell cilia via endosomal EphA-processing. *Nat. Commun.* **10**, 5686 (2019).
16. B. Thorens *et al.*, Ins1(Cre) knock-in mice for beta cell-specific gene recombination. *Diabetologia* **58**, 558–565 (2015).
17. C. J. Haycraft *et al.*, Intraflagellar transport is essential for endochondral bone formation. *Development* **134**, 307–316 (2007).
18. S. Jayaraman, A novel method for the detection of viable human pancreatic beta cells by flow cytometry using fluorophores that selectively detect labile zinc, mitochondrial membrane potential and protein thiols. *Cytometry A* **73**, 615–625 (2008).
19. W. S. Head *et al.*, Connexin-36 gap junctions regulate in vivo first- and second-phase insulin secretion dynamics and glucose tolerance in the conscious mouse. *Diabetes* **61**, 1700–1707 (2012).
20. I. Konstantinova *et al.*, EphA-ephrin-A-mediated  $\beta$  cell communication regulates insulin secretion from pancreatic islets. *Cell* **129**, 359–370 (2007).
21. R. K. P. Benninger, D. W. Piston, Cellular communication and heterogeneity in pancreatic islet insulin secretion dynamics. *Trends Endocrinol. Metab.* **25**, 399–406 (2014).
22. P. Bergsten, E. Grapengiesser, E. Gylfe, A. Tengholm, B. Hellman, Synchronous oscillations of cytoplasmic Ca<sup>2+</sup> and insulin release in glucose-stimulated pancreatic islets. *J. Biol. Chem.* **269**, 8749–8753 (1994).
23. J. E. Ayala *et al.*; NIH Mouse Metabolic Phenotyping Center Consortium, Standard operating procedures for describing and performing metabolic tests of glucose homeostasis in mice. *Dis. Model. Mech.* **3**, 525–534 (2010).
24. Z. Anvarian, K. Mykityn, S. Mukhopadhyay, L. B. Pedersen, S. T. Christensen, Cellular signalling by primary cilia in development, organ function and disease. *Nat. Rev. Nephrol.* **15**, 199–219 (2019).
25. T. Eguether, F. P. Cordelieres, G. J. Pazour, Intraflagellar transport is deeply integrated in hedgehog signaling. *Mol. Biol. Cell* **29**, 1178–1189 (2018).
26. E. J. Ezratty *et al.*, A role for the primary cilium in Notch signaling and epidermal differentiation during skin development. *Cell* **145**, 1129–1141 (2011).
27. K. Zimmerman, B. K. Yoder, Snapshot: Sensing and signaling by cilia. *Cell* **161**, 692–692.e1 (2015).
28. J. Hughes, Signaling protein antibody microarray analyses for islets of control and IFT88 knockout mice. Gene Expression Omnibus. <https://www.ncbi.nlm.nih.gov/geo/query/acc.cgi?acc=GSE138885>. Deposited 15 October 2019.
29. J. Hughes, Phospho-antibody microarray analyses for islets of control and IFT88 knockout mice. Gene Expression Omnibus. <https://www.ncbi.nlm.nih.gov/geo/query/acc.cgi?acc=GSE138856>. Deposited 15 October 2019.
30. Q. Li *et al.*, A cullin 4B-RING E3 ligase complex fine-tunes pancreatic  $\delta$  cell paracrine interactions. *J. Clin. Invest.* **127**, 2631–2646 (2017).
31. C. Dai *et al.*, Pancreatic islet vasculature adapts to insulin resistance through dilation and not angiogenesis. *Diabetes* **62**, 4144–4153 (2013).
32. M. F. Hogan *et al.*, Markers of islet endothelial dysfunction occur in male B6.BKS(D)-Leprdb/J mice and may contribute to reduced insulin release. *Endocrinology* **158**, 293–303 (2017).
33. A. Rabinovitch, W. L. Suarez-Pinzon, O. Sorensen, R. C. Bleackley, Inducible nitric oxide synthase (iNOS) in pancreatic islets of nonobese diabetic mice: Identification of iNOS-expressing cells and relationships to cytokines expressed in the islets. *Endocrinology* **137**, 2093–2099 (1996).
34. H. Sase, T. Watabe, K. Kawasaki, K. Miyazono, K. Miyazawa, VEGFR2-PLCgamma1 axis is essential for endothelial specification of VEGFR2+ vascular progenitor cells. *J. Cell Sci.* **122**, 3303–3311 (2009).
35. T. Takahashi, S. Yamaguchi, K. Chida, M. Shibuya, A single autophosphorylation site on KDR/Flk-1 is essential for VEGF-A-dependent activation of PLC-gamma and DNA synthesis in vascular endothelial cells. *EMBO J.* **20**, 2768–2778 (2001).
36. E. Lin, P.-H. Kuo, Y.-L. Liu, A. C. Yang, S.-J. Tsai, Transforming growth factor- $\beta$  signaling pathway-associated genes SMAD2 and TGFBR2 are implicated in metabolic syndrome in a Taiwanese population. *Sci. Rep.* **7**, 13589 (2017).
37. A. Sjöholm, C. Hellerström, TGF-beta stimulates insulin secretion and blocks mitogenic response of pancreatic beta-cells to glucose. *Am. J. Physiol.* **260**, C1046–C1051 (1991).
38. B. Sorrensen *et al.*, A critical role for  $\beta$ -catenin in modulating levels of insulin secretion from  $\beta$ -cells by regulating actin cytoskeleton and insulin vesicle localization. *J. Biol. Chem.* **291**, 25888–25900 (2016).
39. L. Velazco-Cruz *et al.*, Acquisition of dynamic function in human stem cell-derived  $\beta$  cells. *Stem Cell Reports* **12**, 351–365 (2019).
40. X. Geng *et al.*,  $\alpha$ -Synuclein binds the K(ATP) channel at insulin-secretory granules and inhibits insulin secretion. *Am. J. Physiol. Endocrinol. Metab.* **300**, E276–E286 (2011).
41. R. Kapeller, R. Chakrabarti, L. Cantley, F. Fay, S. Corvera, Internalization of activated platelet-derived growth factor receptor-phosphatidylinositol-3' kinase complexes: Potential interactions with the microtubule cytoskeleton. *Mol. Cell. Biol.* **13**, 6052–6063 (1993).
42. W. J. Gan *et al.*, Local integrin activation in pancreatic  $\beta$  cells targets insulin secretion to the vasculature. *Cell Rep.* **24**, 2819–2826.e3 (2018).
43. E. E. Charrier *et al.*, Desmin mutation in the C-terminal domain impairs traction force generation in myoblasts. *Biophys. J.* **110**, 470–480 (2016).
44. D. Günzel, A. S. L. Yu, Claudins and the modulation of tight junction permeability. *Physiol. Rev.* **93**, 525–569 (2013).
45. H. Li *et al.*, Paradoxical overexpression and translocation of connexin43 in homocysteine-treated endothelial cells. *Am. J. Physiol. Heart Circ. Physiol.* **282**, H2124–H2133 (2002).
46. W. Roell *et al.*, Overexpression of Cx43 in cells of the myocardial scar: Correction of post-infarct arrhythmias through heterotypic cell-cell coupling. *Sci. Rep.* **8**, 7145 (2018).
47. M. Braun *et al.*, Voltage-gated ion channels in human pancreatic beta-cells: Electrophysiological characterization and role in insulin secretion. *Diabetes* **57**, 1618–1628 (2008).
48. L. E. Fridlyand, D. A. Jacobson, L. H. Philipson, Ion channels and regulation of insulin secretion in human  $\beta$ -cells: A computational systems analysis. *Islets* **5**, 1–15 (2013).
49. P. K. Dadi *et al.*, Inhibition of pancreatic  $\beta$ -cell Ca<sup>2+</sup>/calmodulin-dependent protein kinase II reduces glucose-stimulated calcium influx and insulin secretion, impairing glucose tolerance. *J. Biol. Chem.* **289**, 12435–12445 (2014).
50. B. J. Galletta *et al.*, Drosophila pericentrin requires interaction with calmodulin for its function at centrosomes and neuronal basal bodies but not at sperm basal bodies. *Mol. Biol. Cell* **25**, 2682–2694 (2014).
51. O. Kluth *et al.*, Decreased expression of cilia genes in pancreatic islets as a risk factor for type 2 diabetes in mice and humans. *Cell Rep.* **26**, 3027–3036.e3 (2019).
52. M. Benzinou *et al.*, Bardet-Biedl syndrome gene variants are associated with both childhood and adult common obesity in French Caucasians. *Diabetes* **55**, 2876–2882 (2006).
53. M. F. Brereton *et al.*, Hyperglycaemia induces metabolic dysfunction and glycogen accumulation in pancreatic  $\beta$ -cells. *Nat. Commun.* **7**, 13496 (2016).
54. M. S. Remedi *et al.*, Secondary consequences of  $\beta$  cell inexcitability: Identification and prevention in a murine model of K(ATP)-induced neonatal diabetes mellitus. *Cell Metab.* **9**, 140–151 (2009).
55. Z. Wang, N. W. York, C. G. Nichols, M. S. Remedi, Pancreatic  $\beta$  cell dedifferentiation in diabetes and redifferentiation following insulin therapy. *Cell Metab.* **19**, 872–882 (2014).
56. B. Svendsen *et al.*, Insulin secretion depends on intra-islet glucagon signaling. *Cell Rep.* **25**, 1127–1134.e2 (2018).
57. S. M. Guadiana *et al.*, Type 3 adenyllyl cyclase and somatostatin receptor 3 expression persists in aged rat neocortical and hippocampal neuronal cilia. *Front. Aging Neurosci.* **8**, 127 (2016).
58. T. Iwanaga, T. Miki, H. Takahashi-Iwanaga, Restricted expression of somatostatin receptor 3 to primary cilia in the pancreatic islets and adenohypophysis of mice. *Biomed. Res.* **32**, 73–81 (2011).

59. X. P. Wang *et al.*, SSTR5 ablation in islet results in alterations in glucose homeostasis in mice. *FEBS Lett.* **579**, 3107–3114 (2005).
60. D. Bosco *et al.*, Unique arrangement of alpha- and beta-cells in human islets of Langerhans. *Diabetes* **59**, 1202–1210 (2010).
61. M. Brissova *et al.*, Assessment of human pancreatic islet architecture and composition by laser scanning confocal microscopy. *J. Histochem. Cytochem.* **53**, 1087–1097 (2005).
62. R. A. E. Drigo *et al.*, Structural basis for delta cell paracrine regulation in pancreatic islets. *Nat. Commun.* **10**, 1–12 (2019).
63. P. G. DeCaen, M. Delling, T. N. Vien, D. E. Clapham, Direct recording and molecular identification of the calcium channel of primary cilia. *Nature* **504**, 315–318 (2013).
64. M. Delling, P. G. DeCaen, J. F. Doerner, S. Febvay, D. E. Clapham, Primary cilia are specialized calcium signalling organelles. *Nature* **504**, 311–314 (2013).
65. S. M. Nauli, R. Pala, S. J. Kleene, Calcium channels in primary cilia. *Curr. Opin. Nephrol. Hypertens.* **25**, 452–458 (2016).
66. P. Rorsman, M. Braun, Q. Zhang, Regulation of calcium in pancreatic  $\alpha$ - and  $\beta$ -cells in health and disease. *Cell Calcium* **51**, 300–308 (2012).
67. D. M. Nathan *et al.*; American Diabetes Association, Impaired fasting glucose and impaired glucose tolerance: Implications for care. *Diabetes Care* **30**, 753–759 (2007).
68. J. J. Malicki, C. A. Johnson, The cilium: Cellular antenna and central processing unit. *Trends Cell Biol.* **27**, 126–140 (2017).
69. R. Nanjundappa *et al.*, Regulation of cilia abundance in multiciliated cells. *eLife* **8**, e44039 (2019).
70. S. Wang, M. J. Livingston, Y. Su, Z. Dong, Reciprocal regulation of cilia and autophagy via the MTOR and proteasome pathways. *Autophagy* **11**, 607–616 (2015).
71. P. E. Lacy, M. Kostianovsky, Method for the isolation of intact islets of Langerhans from the rat pancreas. *Diabetes* **16**, 35–39 (1967).
72. A. Ustione, D. W. Piston, Dopamine synthesis and D3 receptor activation in pancreatic  $\beta$ -cells regulates insulin secretion and intracellular  $[Ca^{2+}]$  oscillations. *Mol. Endocrinol.* **26**, 1928–1940 (2012).
73. A. I. Mina *et al.*, CalR: A web-based analysis tool for indirect calorimetry experiments. *Cell Metab.* **28**, 656–666.e1 (2018).
74. M. H. Tschöp *et al.*, A guide to analysis of mouse energy metabolism. *Nat. Methods* **9**, 57–63 (2011).
75. R. F. Laine *et al.*, NanoJ: A high-performance open-source super-resolution microscopy toolbox. *J. Phys. D Appl. Phys.* **52**, 163001 (2019).
76. S. Babicki *et al.*, Heatmapper: Web-enabled heat mapping for all. *Nucleic Acids Res.* **44**, W147–W153 (2016).
77. M. V. Kuleshov *et al.*, Enrichr: A comprehensive gene set enrichment analysis web server 2016 update. *Nucleic Acids Res.* **44**, W90–W97 (2016).